Design Study Evaluating Impact of Gap Loss on Inductors with Nanocrystalline Cores

by

Maurice Sturdivant

B.S. Electrical Engineering, University of Pittsburgh, 2022

Submitted to the Graduate Faculty of

the Swanson School of Engineering in partial fulfillment

of the requirements for the degree of

Master of Science

University of Pittsburgh

2024

UNIVERSITY OF PITTSBURGH

SWANSON SCHOOL OF ENGINEERING

This thesis was presented

by

Maurice Sturdivant

It was defended on

May 21st, 2024

and approved by

Mohamed Bayoumy, Ph.D., Assistant Professor, Department of Electrical and Computer Engineering

Robert Kerestes, Ph.D., Associate Professor, Department of Electrical and Computer Engineering

Thesis Advisor: Brandon Grainger, Ph.D., Associate Professor, Eaton Faculty Fellow, Department of Electrical and Computer Engineering

Thesis Advisor: Paul Ohodnicki, Jr., Ph.D., Associate Professor, Department of Mechanical Engineering and Materials Science

Design Study Evaluating Impact of Gap Loss on Inductors with Nanocrystalline Cores

Maurice Sturdivant, M.S.

University of Pittsburgh, 2024

As decarbonization efforts continue and electric vehicle (EV) technology matures, engineers are challenged with developing compact and efficient power electronics. Magnetic components, including inductors, are critical to the operation of power conversion systems. To increase power density and efficiency, it is ideal to 1) reduce the size of magnetic components, as they are often the largest contributors to the system's physical footprint, and 2) minimize component power losses. A common inductor design technique is placing an air gap in the core, allowing designers to tune the inductance and allow higher levels of magnetic field without saturation. The inclusion of gaps can increase the total magnetic core loss beyond those predicted by common models such as the Steinmetz equation, creating the need for accurate gap loss models. In this study, finite-element simulation and physical experiments are used to validate assumptions about the sources of gap loss and its dependence on gap length. A sample nanocrystalline inductor is tested over a range of gap lengths under fixed operating conditions, with core losses measured and compared to a selected gap loss model. The model was then integrated into a multi-objective optimization framework to study the fitness of nanocrystalline cores against ferrite cores at different switching frequencies. This work finds that gap losses can increase the total loss of nanocrystalline inductors by up to an order of magnitude as frequency increases, implying that consideration of gap losses is vital to selecting the appropriate core material for design applications.

Keywords: core loss, inductors, air gaps, nanocrystalline, loss measurement, optimization.

Table of Contents

List of Tables

List of Figures

Preface

I would like to thank my co-advisors, Dr. Brandon Grainger and Dr. Paul Ohodnicki, Jr., for their mentorship as both research advisors and educators. Dr. Grainger's continued guidance has been an integral part of my electrical engineering education at the undergraduate and graduate levels. Dr. Ohodnicki's support has also been pivotal in learning the importance of magnetics in the field of electric power. I would also like to recognize Christoper Bracken, Dr. Ryan Brody, and Dr. Mohendro Ghosh for providing technical knowledge and support throughout my graduate research experience.

I would like to personally thank Sabrina Helbig, Todd Marzec, and my peers in the Electric Power Technologies Lab for their fellowship and encouragement throughout graduate school. Thank you to my friends and family for their continued love and support over the last six years, as it provided me with the tools to navigate the challenges encountered both in life and in school.

This work was supported and funded by Department of Energy (DOE) Vehicle Technology Office and the Swanson School of Engineering Graduate Engineering Education Scholarship (GEES).

1.0 Introduction

With the acceleration of electric vehicle (EV) development and integration, power electronics engineers are challenged with supporting this transition. Within a single vehicle, several power electronic converters are needed to interface with its electric motor, batteries, auxiliary electronic loads, and the power grid, requiring their physical footprint and operating temperatures to be minimized. Power conversion systems will also be crucial to building the charging infrastructure needed to make EVs a more practical alternative to internal combustion engine vehicles. The widespread adoption of EVs and off-board charging systems has created the need for compact and efficient power electronic systems.

Power density and efficiency are key metrics driving the design of power electronic conversion systems. The Department of Energy has set targets to develop converters reaching power density of 100 kW/L and efficiency of 98% as soon as 2025 [1]. A common approach to reducing the size of converters is to use high frequencies (>50 kHz), enabled by advances in wide band-gap semiconductor devices such as silicon-carbide (SiC) and gallium nitride (GaN) [3]. These higher switching frequencies increase power losses and heating in the converter's conductors and magnetic components, such as inductors. Inductors are critical to the operation of power electronic converters, able to serve as energy storage elements, provide DC filtering, and enable soft-switching techniques (zero-current switching, zero-voltage switching).

In addition to frequency, inductors are impacted by other design characteristics, including the winding, core material, and inclusion of an air gap. To effectively balance power density and efficiency, it is important to accurately predict losses in these components.

1.1 Sources of Power Loss in Inductors

Power is dissipated in both the winding and the magnetic core of an inductor. Inductor winding losses consist of 1) resistive losses in the conductor, 2) additional losses due to skin effect, which can increase current density at the outer surface of conductors, and 3) losses due to proximity effect, which is eddy current induced in the winding by nearby magnetic fields. While the resistive losses are only impacted by the excitation current flowing through the winding, the skin effect and proximity losses are frequency-dependent losses.

Magnetic core losses are categorized as classical eddy current loss and hysteresis loss. Classical eddy current losses are the resistive losses caused by magnetic flux-induced eddy currents in the core material depicted in Figure 1 [20]. While this is a component of loss in magnetic cores, it is a form of loss that can be observed in any electrically conductive material. Conversely, hysteresis losses are primarily seen in magnetic materials. As a magnetic field is applied to a magnetic material, the domains that compose the material begin to align, shown in Figure 2 [23]. The movement of the magnetic domains is restricted by the material's atomic structure, so energy is needed to overcome these physical restrictions. The energy consumed as the domain walls are moved by this field results in hysteresis loss. Since they are the product of the component's magnetizing flux passing through the core, classical eddy current loss and hysteresis will be collectively referred to as magnetizing core loss.

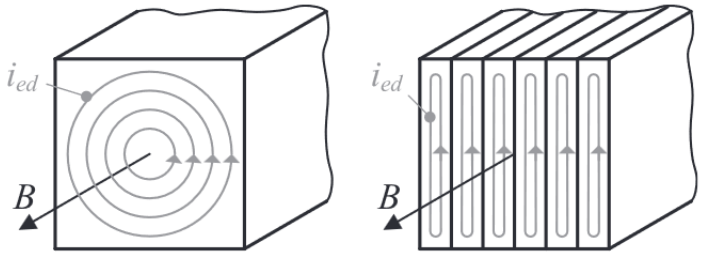

Figure 1: Eddy Currents Induced by Magnetizing Flux in Solid Core (left) and Laminated Core (right) [20]

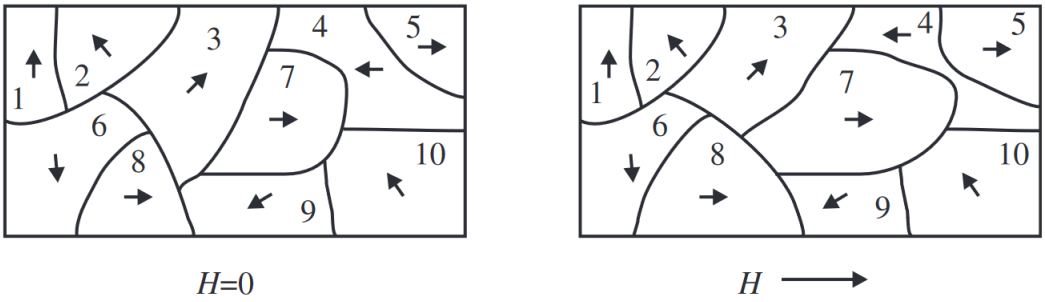

Figure 2: Magnetic Domain Walls Before (left) and After (right) Magnetic Field is Applied [23]

1.2 Magnetic Equivalent Circuits

An important concept for magnetic component design and analysis is the magnetic equivalent circuit (MEC). From Ampere's Law, which relates current to the field intensity over a closed path, the relationship between magnetomotive force (MMF), current, and the number of conductors can be established. From this relationship comes Kirchoff's voltage law for magnetic circuits, an analogue to Kirchoff's voltage law for electric circuits, which states that the sum of MMF drops over a closed path is equivalent to the sum of MMF sources [23]. In magnetic devices such as inductors and transformers, a winding with N conductor turns carrying i amps of current produces a magnetomotive force F equal to:

$$F = Ni \tag{1.1}$$

According to Gauss's Law, the surface integral of magnetic flux over a closed volume is zero. This allows for the development of Kirchoff's flux law for magnetic circuits, which states that the sum of fluxes into or out of any magnetic circuit node is zero [23]. This law parallels Kirchoff's current law for electric circuits, stating that the sum of electrical currents flowing into and out of a node is zero. The final law of magnetic equivalent circuits

is Ohm's Law for magnetic circuits, relating the properties of magnetic materials to the flux passing through them and the MMF drops across them. For a sample of magnetic material with reluctance R and flux Φ passing through it, the MMF drop F across the sample can be expressed with (1.2).

$$F = R\Phi \tag{1.2}$$

With these connections to current and voltage in electrical circuits established, the magnetic circuit can be fully realized. While inductors are often thought of as a single component in electrical circuit representations, the magnetic circuit individually represents the winding and core segments. The current in the winding is a source of magnetomotive force that causes magnetic flux to flow through core. The core material's permeability and physical dimensions determine its reluctance, which affects the change in MMF as flux passes through it. Table 1 lists the quantities in an MEC, along with the electrical circuit analogue, and Figure 3 pictures a sample MEC. These circuits are useful tools, as they can be used to estimate key design values, such as flux density, inductance, and core loss.

Table 1: Magnetic Circuit Values and Electrical Counterparts

Symbol	**Quantity**	**Electrical Analogue**
F	Magnetomotive Force (MMF)	Electromotive Force (EMF)
R	Reluctance	Resistance
Φ	Magnetic Flux	Current

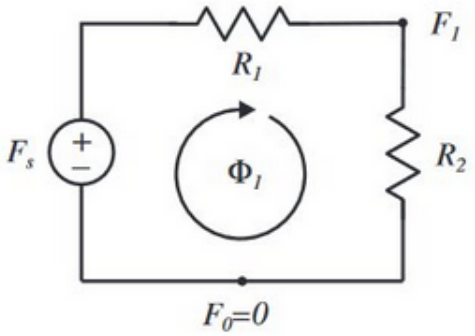

Figure 3: Sample Magnetic Equivalent Circuit [23]

1.3 Air Gaps and Impacts on Loss

Cutting and placing air gaps in cores is a common design technique, as it provides a way to tune the inductance of the components and allows higher levels of magnetization without saturating the core [14]. Since air has much lower permeability than the magnetic core, the insertion of an air gap creates a high reluctance element in the magnetic circuit. Because of this change in permeability, air gaps cause magnetic flux in the core to spread out, or fringe, around it. The portion of flux that passes straight through the gap is direct gap flux, while the flux that moves around the gap is fringing flux, shown in Figure 4.

Since portions of flux take different paths around the air gap, each one can be represented with separate, parallel reluctance values. R_{gd} refers to the direct gap flux, while R_{foc}, R_{fic}, and R_{ff} refer to the fringing fluxes. In Figure 4, R_{foc} is the flux that fringes left, around the outer edge of the core, while R_{fic} is the portion fringing right, inside the area enclosed by the core. R_{ff} refers to the two fringing flux paths that would be flowing perpendicular to R_{foc} and R_{fic}. Not pictured in Figure 4, one of these flux paths would be travelling into the page, or behind the core, and the other out of the page, or in front of the core. Figure 4 also shows the MEC representation of the gap flux paths, which resembles a parallel combination of resistances.

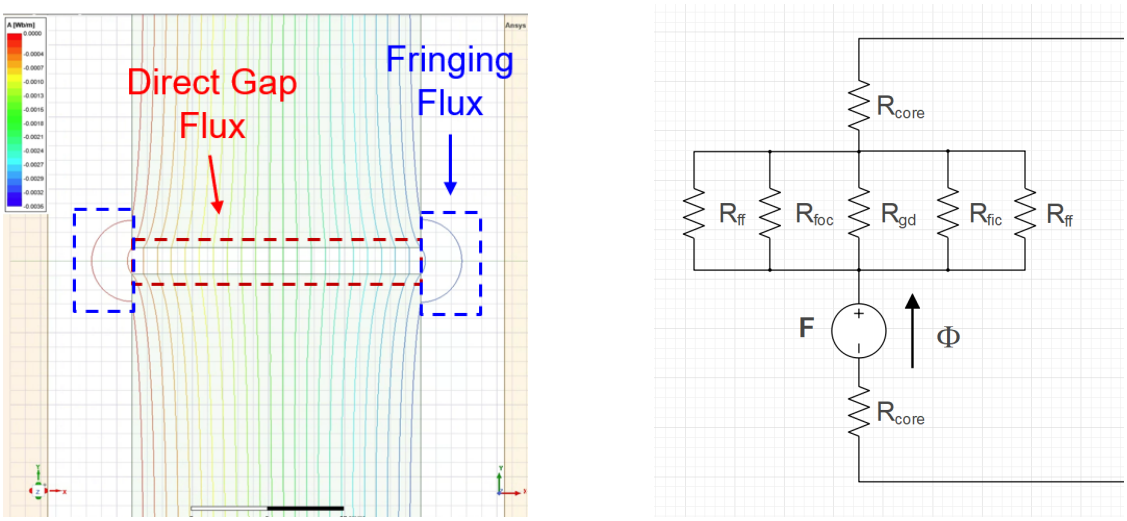

Figure 4: Air Gap Flux Paths (left) and MEC Representation (right)

In addition to the magnetizing losses previously discussed, inductors begin to experience increases in loss after being cut and having air gaps placed between the core halves. While these localized losses near the core gap are generally referred to as gap losses, they are the result of different mechanisms. The first source of gap loss is the result of damage inflicted by machining processes. In other literature, it has been shown that the cut surfaces of the core facing the air gap can experience increased loss density [18]. In ferrite cores, this damage is thought to cause higher hysteresis losses on the gap faces. In laminated nanocrystalline cores, however, this cutting can create short circuits between conductive lamination sheets, increasing eddy current losses on the gap face [10]. Since these gap losses occur on the surface of the core gap, normal to the path of the direct gap flux, this will be referred to as direct gap loss.

The other form of gap loss explored in this work is fringing gap loss. The components of fringing flux normal to a core's lamination surface induce additional eddy currents, resulting in localized losses near the edges of the air gap [9]. It is important to distinguish this localized loss from the classical eddy current losses induced throughout the entire core by magnetizing flux. While this work is focused on core loss, designing a gapped inductor can also impact winding loss. When windings are placed near the air gap, the fringing flux can pass through the conductors, contributing to proximity winding loss [4].

1.4 Core Materials

An important aspect of inductor design is core material selection. The permeability, saturation flux density, electrical conductivity, and weight all contribute to the performance of an inductor. Designs with high permeability and saturation points can be excited with higher levels of current and magnetic flux, which is important for high power applications. As previously stated, eddy current losses are a significant component of core loss in magnetic devices that can increase significantly with both flux density and frequency. When operating at higher frequencies, understanding the conductivity of the material will help predict the magnitude of the eddy current loss. Since miniaturizing components is a common design goal, designers often look for materials that will result in smaller and lighter designs. While there are many classes of magnetic core materials, this work is primarily concerned with two: nanocrystalline cores and ferrite cores.

An example ferrite core and nanocrystalline core are pictured in Figure 5 [11]. Ferrite cores are composed of a metal-oxide ceramic material and solid in structure, corresponding to the core pictured in the lefthand side of Figure 1. While these cores saturate at lower flux densities than nanocrystalline cores, they are highly resistive. This results in significantly lower eddy current losses than many other core material options, making them suitable for use at high frequencies. Nanocrystalline cores are a class of magnetic materials composed of thin laminations or ribbons of metallic-glass material, reflected in the righthand side of Figure 1. Because of the layered structure created by these laminations, they are often referred to as tapewound cores. These cores offer high saturation flux densities, often above 1 Tesla (T) [28], and high thermal conductivity [21], making them attractive options for high power applications. Due to the conductive nature of the laminations, eddy current losses can often become a limiting factor for these materials [11].

Figure 5: Ferrite Core (left) and Nanocrystalline Core (right) [11]

1.5 Contribution of this Work and Organization of Thesis

The contribution of this work is a study investigating the impact of air gap length on gap losses in a cut nanocrystalline inductor core. By testing an inductor core sample at different set gap lengths, the effects of eddy current losses induced by fringing flux around the air gap can be analyzed independently of the losses caused by the core-cutting process. The final goal is to integrate a gap loss model into a multi-objective optimization framework, providing insights on the impact of gap loss on the fitness of nanocrystalline cores against other core materials.

Section 2 describes common core loss models, including a model proposed in literature to predict fringing gap loss in nanocrystalline cores. Section 3 discusses the use of finite element analysis (FEA) to visualize magnetic fields in a nanocrystalline core and validate assumptions about sources of gap loss. Section 4 details the experiments conducted to measure core losses with respect to gap length. Section 5 discusses the optimization work, with a comparison of results between inductors designed neglecting gap loss and designs created after integrating the selected gap loss models.

2.0 Core Loss Models

Different approaches to modeling losses in magnetic cores are discussed in this section. There are several factors contributing to power losses in magnetic cores, making it difficult to accurately calculate. This problem has been approached using several methods, resulting in the development of multiple core loss models. Many of these models were only developed considering loss due to magnetizing flux and lack ways to estimate the impact of air gaps on core loss.

This section is organized as such: first, common core loss models are reviewed, with an emphasis on the Steinmetz Equation. Then, models presented in literature to predict direct gap loss and fringing gap loss are covered.

2.1 Traditional Core Loss Models

The most common approach to modeling magnetizing core losses is through empirical models, often using the equation developed by Charles Steinmetz [19]. The Steinmetz equation (SE), shown in (2.1), uses a power function to relate the core loss to the frequency f and peak flux density B_m. Curves are fitted to measured core loss data, yielding the coefficients k, α, and β [23]. This equation assumes sinusoidal excitations [19], so it is not as accurate in power electronics applications where square waves and other non-sinusoidal signals are used.

$$P_{c|SE} = k f^{\alpha} B_m^{\beta} \tag{2.1}$$

Other models have been developed from the Steinmetz Equation to account for its limitations, including the Modified Steinmetz equation (MSE), shown in (2.2). This form of the equation accounts for nonsinusoidal excitations by relating core loss to the change in

flux density $\triangle B$ and an equivalent frequency of the waveform f_{eq}, calculated using (2.3) [29]. Other notable models built on the original Steinmetz equation are the Generalized Steinmetz equation (GSE), the Improved Generalized Steinmetz equation (iGSE), and the Natural Steinmetz Extension (NSE) [25].

$$P_{c|MSE} = (k f_{eq}^{\alpha-1} B_m^{\beta}) f \tag{2.2}$$

$$f_{eq} = \frac{2}{\triangle B^2 \pi^2} \int_0^T (\frac{dB}{dt})^2 dt \tag{2.3}$$

As discussed in Section 1, magnetizing core losses are caused by different mechanisms, including hysteresis loss and classical eddy current loss. A common type of core loss model built on this understanding is the loss separation model. Loss separation models individually calculate the contributions of hysteresis loss and classical eddy current losses to the core's total loss. Over time, this model has been developed to include a third component, referred to as anomalous or excess loss [5, 19]. The anomalous loss term was introduced to account for additional eddy current losses due to nonuniform magnetization processes within the core, including domain wall movement, not captured by the classical eddy current loss term [16].

$$P_c = k_h f B_m^{\beta} + k_c f^2 B_m^2 + k_e f^{1.5} B_m^{1.5} \tag{2.4}$$

The simulation tool used in Section 3 and experimental setup described in Section 4 utilize sinusoidal excitations. Also, the gap loss models explored in this work most closely follow the structure of the original Steinmetz Equation. Therefore, the original Steinmetz equation is used to estimate magnetizing core losses in this work.

2.2 Gap Loss Models

Significant work has been done to model magnetic core loss under different conditions, including non-sinusoidal excitations and DC bias. As discussed, there are models that separately estimate the contributions of hysteresis loss, classical eddy current loss, and anomalous loss. Despite there being an abundance of core loss models to choose from, they are primarily concerned with loss mechanisms associated with the core's magnetizing flux. The following models aim to predict the additional losses caused by the introduction of gaps in magnetic cores.

2.2.1 Direct Gap Loss

The first of these models is concerned with estimating the increased loss density on the gap-facing surfaces of ferrite cores, or direct gap loss. To minimize the radius of fringing flux paths and associated proximity winding effects, some cores use several, smaller gaps that sum to the desired gap length [18]. While this method reduces the amount of fringing flux passing through the windings, the use of multiple, smaller gaps means that the core will be cut in more places, resulting in more damaged, or ground, surface regions that will experience increased hysteresis loss. A section of a cut ferrite core is pictured in Figure 6, showing the separate bulk and surface regions [18]. d_b and d_s denote the thickness of the bulk region and surface region, respectively. This modeling approach assumes that the thickness of the surface region is negligible relative to that of the bulk region, so that $d_b + 2d_s \approx d_b$.

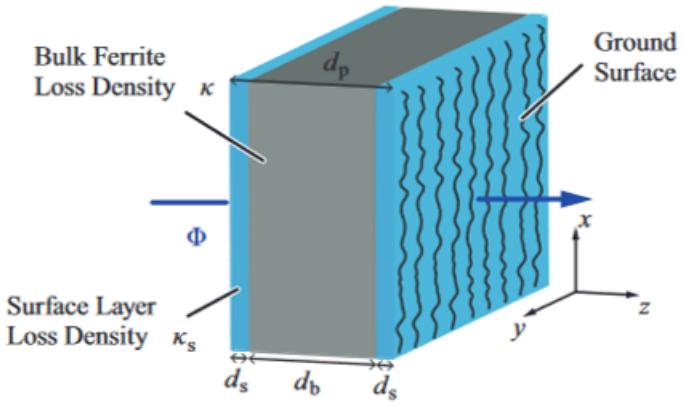

Figure 6: Ferrite Core Segment with Ground Surface [18]

To account for direct gap loss on the ground surface, Neumayr et al. use separate sets of coefficients for the two regions of a Manganese-Zinc (MnZn) ferrite core [18]. Following the format of the Steinmetz equation, the coefficients for the bulk region are k, α, and β, resulting in a volumetric power loss density p_{bulk}, in units of W/m^3. The bulk region coefficients are the same as those supplied by the vendor for the core material. Since the surface region is assumed to be of negligible thickness, the surface region coefficients k_s, α_s, and β_s yield a two-dimensional loss density p_{surf}, in units of W/m^2. Total losses can be obtained from these loss densities by multiplying them with the total core volume and total ground surface area, respectively. The bulk and surface coefficients for the ferrite core examined in [18] are listed in Table 2.

Table 2: Steinmetz Coefficients for Bulk and Surface Regions of Ferrite Core

Bulk		**Surface**	
k	13.2 W/m^3	k_s	0.272 W/m^2
α	1.36	α_s	1.13
β	2.77	β_s	2.9

To estimate the magnetizing loss in the MnZn ferrite core tested in [18], the total bulk core loss, P_{bulk}, should be calculated. Calculating the total surface loss P_{surf}, corresponds to the direct gap loss associated with a single gap, or the two ground surfaces enclosing the gap. This value should be multiplied by the number of discrete gaps in the core, as each gap will require another cut in the core, resulting in another pair of ground surfaces on the core's cross-section. The equations for bulk loss and surface loss are shown in (2.5) and (2.6).

$$P_{bulk} = k f^{\alpha} B^{\beta} V_{core} \tag{2.5}$$

$$P_{surf} = 2 k_s f^{\alpha_s} B^{\beta_s} A_e \tag{2.6}$$

2.2.2 Fringing Gap Loss

The primary focus of this work is to evaluate the impact of fringing gap losses observed in nanocrystalline inductor cores, or the eddy current losses induced by fringing flux normal to the core's laminations. The gap loss model used to estimate this, proposed by Wang et al. in [28], was developed from a series of finite element simulations used to model the losses associated with this fringing flux on a gapped, UU-core inductor. The material selected for the development of this model was Finemet, a common nanocrystalline core material.

In these simulation models, both the cores and windings are modeled. The windings are excited with sinusoidal currents to generate magnetic flux, allowing specific flux density values to be reached in the core. To minimize potential proximity effects in the winding, they are spaced away from the core by the gap length l_g. The eddy current losses in the core due to fringing flux were simulated independently of those caused by magnetizing flux, allowing direct calculation of gap losses. The approach used to isolate the fringing gap loss from the classical eddy current loss associated magnetizing flux will be detailed further in Section 4.

The resulting empirical model is similar in structure to the Steinmetz Equation, but includes additional terms to represent the dependence of the fringing gap loss P_g on both the length of the air gap l_g and the width of the lamination strips D, each with their own power coefficients. The finite element models used by Wang et al. tested the sensitivity of the fringing gap loss to changing gap lengths from 1 mm to 2.6 mm, frequencies from 40 kHz to 200 kHz, peak flux densities from 0.1 T to 0.2 T, and lamination widths from 20 mm to 35 mm [28].

Wang et al. used curve-fitting to calculate the coefficients for each of the model's input variables. The power function coefficients for the frequency, peak flux density, and lamination width, k_f, k_{B_m}, and k_D, were determined to be 1.72, 2, and 1.65, respectively. For the simulations conducted, the gap loss was observed to be directly proportional to the gap length, making the power coefficient k_{l_g} equal to 1. Another proportional coefficient k_g, with a value of 1.663e-3, is included in the model. The complete empirical model is shown in (2.7). Unlike the other models discussed so far, this equation yields a total loss in units of Watts, not a loss density. In addition to simulation models, this model has been used to predict gap losses in multiple inductor designs under various operating conditions [7, 22, 28].

$$P_g = k_g l_g f^{k_f} B^{k_{B_m}} D^{k_D} \tag{2.7}$$

3.0 Finite Element Modeling of Gapped Inductors

Finite element analysis software is a powerful tool that enables simulation of the physics in magnetic devices. By allowing users to create two- and three-dimensional geometries and define specific material characteristics, these tools allow designs to be precisely modeled and analyzed. This is done by creating a mesh for the geometries constructed, or a series of smaller shapes that the solution is solved over. This approach allows for the qualitative study of fields and other properties in the design during operation, such as power loss, current density, and flux density.

Ansys Maxwell, a high-performance electromagnetic simulation software package, was used to simulate inductors and analyze the electromagnetic behavior in the cores. Maxwell offers several solvers, capable of solving both electric and magnetic fields in the time domain, the frequency domain, or under DC conditions. Since this work is concerned with magnetic behavior sensitive to switching frequency, the Eddy Current Solver, or the solver designed for solving magnetic fields in the frequency domain, was selected. This solver assumes sinusoidal current excitations at a specified frequency, without DC bias. A distinct advantage this solver offers is the use of an adaptive mesh, an approach that generates a mesh with varying fineness, focusing more on regions with more complex geometries or nonuniform field distributions. To verify the behavior of the fringing fluxes near the gap, the ability to refine the mesh in select areas of the core will be needed. The goal of creating finite element inductor models is to validate the working assumption that, for a fixed flux density and frequency, an increasing gap length causes increased gap loss.

3.1 Model Development

To establish capability using the tool, a sample 100 uH inductor design was selected for simulation. Like the inductor FEA models used to develop the fringing gap loss model discussed in Section 2, this design uses a gapped UU-core. The 3D geometry of this design

was constructed in Ansys Maxwell. First, the core was created using the dimensions listed in Table 5, corresponding to the diagram for a UU-core in Figure 12 [2]. Then, two separate objects were created to represent the winding: one placed around each of the core's legs, centered vertically around the air gap. This winding placement mirrors that of many UU-core inductors, where a winding with N turns has $N/2$ turns placed around each half of the core, minimizing leakage flux and ensuring even flux distribution throughout the core. The last object created was a box enclosing the other geometries, creating a boundary and region for the tool to solve fields in. The complete geometry of the inductor model is shown in Figure 7.

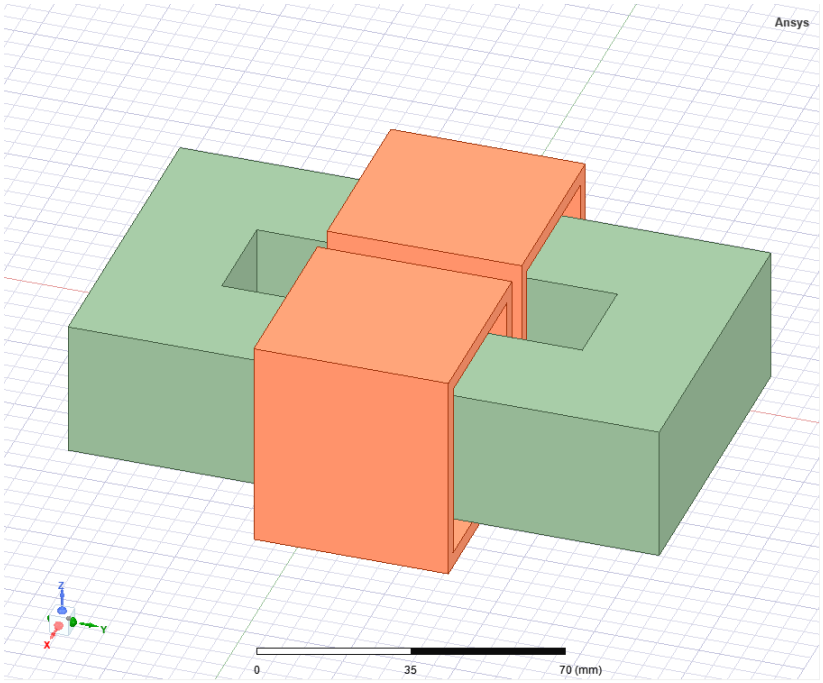

Figure 7: Inductor Model Geometry

After creating the geometry, the different objects were assigned the appropriate materials. The nanocrystalline core material, Finemet FT-3TL, was selected for the core material and copper for the winding material. The properties used to define the materials are listed in Table 3. Along with material properties, Ansys Maxwell has additional settings that must be configured for the simulation to solve properly. Core materials can be assigned either an "Electrical Steel" or "Power Ferrite" core loss model. The "Electrical Steel" option allows the

use of the loss separation model in (2.4) to calculate losses, while the "Power Ferrite" option allows the use of the Steinmetz equation in (2.1). Since documented Steinmetz coefficients for a Finemet FT-3TL core were available, the "Power Ferrite" option was selected for the core.

Meanwhile, the conductors can be defined as "Solid" or "Stranded", depending on the application. Choosing the "Solid" option treats each current-carrying object as a separate conductor, which is useful for evaluating behavior such as skin and proximity effect. The "Stranded" option assumes that the winding being used is composed of strands thin enough to neglect those additional effects. The "Stranded" option was chosen for the winding since the sole purpose of the winding in this study is serve as a source of MMF, generating magnetic flux in the core.

Table 3: Material Definitions Used in FEA Model

Material Property/Coefficient	**Finemet FT-3TL**	**Copper**
Type	Core	Winding
Relative Permittivity, ϵ	1	1
Relative Permeability, μ	20505	0.99999
Bulk Conductivity, σ	8.33×10^5 S/m	5.8×10^7 S/m
Mass Density, ρ	7250 kg/m^3	8933 kg/m^3
k	1.663e-05 W/kg	N/A
α	1.57	N/A
β	2.043	N/A

With the geometries created and materials defined, the model must be configured with a current excitation. To excite the winding with current, a cross section must be created to assign the current. Since the winding consists of two objects, the current must be assigned to both. The modeled inductor was designed to have eight turns evenly distributed around the core, carrying 5 A of current. After the proper excitations were assigned to the windings, the model was complete and ready for simulation, provided it passed the internal validation check that Ansys Maxwell performs.

To begin the simulation, the tool generates and solves an initial mesh. Based on the number of mesh elements and the field solution solved, an estimated energy error value is calculated. With each simulation pass, a new mesh is generated to reduce this error. Once the solution converges beneath the desired energy error, the simulation is complete. For this model, the chosen energy error requirement was 1.5%, so that the model can converge to an accurate solution with a reasonable computation time.

When the simulation is finished, the results can be viewed in Maxwell's "Solution Data" tab. The reported inductance value is 104.7 μH, confirming that the model has been set up correctly and is generally behaving as expected. To identify any potential errors in the model, field overlays were generated and inspected. Field overlays are useful analysis tools in Ansys Maxwell that allow the visualization of field distributions over object surfaces.

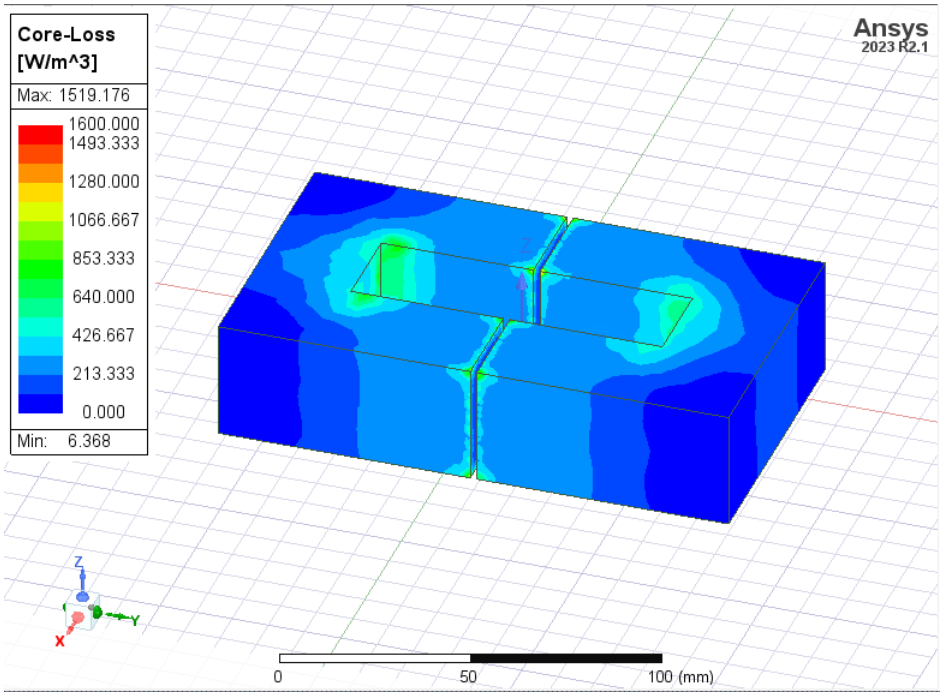

Figure 8: Core Loss Plot for Sample Inductor Model

A field overlay of the core loss in the sample inductor model was created, shown in Figure 8. Near the air gaps, increases in core loss can be observed. While this provides a visual indicator of where losses are dissipated in the core, the losses due to magnetizing flux and fringing flux are both included. Also, the loss increases near the air gap are observed

on the core surfaces facing both the x- and z-directions. This is not consistent with the structure of a tapewound core, where the fringing flux induces eddy currents on faces normal to the lamination stacking direction; in this case, the x-direction. To effectively represent the physical structure of a laminated core material, the model and material definitions must be modified further.

3.2 Anisotropic Properties of Laminated Cores

While solid geometries can be used to model the relative permeability and bulk conductivity of a Finemet core, it does not consider its laminated structure. The laminated structure of the material is inherently anisotropic, meaning that electromagnetic properties vary in relation to the direction that fields are moving through it. Specifically, the permeability and conductivity of the material change significantly between the parallel and normal directions relative to the laminations. Since this study is concerned with the components of fringing flux normal to the surface of the core laminations, the model was modified to both isolate these effects and appropriately represent the anisotropic properties of a tapewound nanocrystalline core.

To model the core anisotropically, the permeability μ and conductivity σ must be separated into normal (μ_n, σ_n) and tangential (μ_t, σ_t) components. Defining these values tells the simulation how to treat fields that are perpendicular and parallel to the laminations, respectively. These values can be calculated using the permeability of free space, μ_0, core stacking factor, F_{stk}, lamination width D, and lamination strip thickness d. The expressions used to calculate these values are listed in (3.1), (3.2), (3.3), and (3.4), consistent with existing approaches to model laminated materials [26]. The resulting anisotropic properties for a laminated Finemet FT-3TL core with a stacking factor of 0.8 and lamination thickness of 17.8 μm are listed in Table 4.

$$\mu_t = F_{stk}\mu + (1 - F_{stk})\mu_0 \tag{3.1}$$

$$\mu_n = \frac{\mu\mu_0}{F_{stk}\mu_0 + (1 - F_{stk})\mu} \tag{3.2}$$

$$\sigma_t = F_{stk}\sigma \tag{3.3}$$

$$\sigma_n = (\frac{d}{D})^2 \frac{1}{F_{stk}}\sigma \tag{3.4}$$

Table 4: Anisotropic Properties of Finemet Core

Relative Permeability		**Conductivity (S/m)**	
μ	20505	σ	833333
μ_t	16404	σ_t	666400
μ_n	5	σ_n	0.5398

The initial model was modified to include the calculated anisotropic permability and conductivity values. Ansys Maxwell allows the permeability and conductivity of materials to be defined in the x-, y-, and z-directions. To appropriately model the laminated core, the core geometry was separated into segments to reflect the different stacking directions. The sections of the core with laminations normal to the x-axis were configured so that μ_x and σ_x were set to μ_n and σ_n, respectively. Since the y- and z-axes are parallel to the lamination sheet, $\mu_{y,z}$ were set to μ_t, while $\sigma_{y,x}$ were set to σ_t. For the section of the core with lamination normal to the y-axis, the y-components of the permeability and conductivity were set to μ_n and σ_n and the x- and z-components were set to μ_t and σ_t.

After incorporating these changes, the simulation was run again. The model's inductance was 103.5 μH, consistent with the original simulation's value. Despite having similar inductance values, the anisotropic material definitions resulted in a finer mesh. The new mesh has its smallest elements concentrated near the gaps and edges of the core, which is better suited for capturing the eddy current effects in the gap region near the surface of the laminations. The number of tetrahedra, or mesh elements, increased from 320,541 to 605,935. The two meshes are pictured in Figure 9.

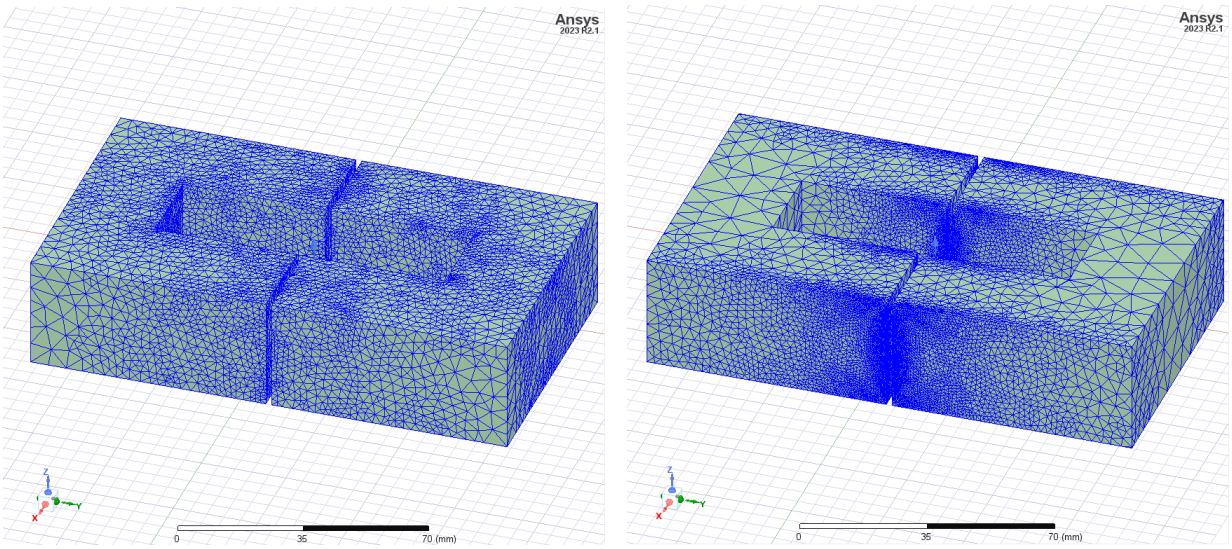

Figure 9: Core Mesh with Isotropic (left) and Anisotropic (right) Material Definition

3.3 Eddy Current Loss Near Air Gap

With a working inductor model and a mesh created for a gapped, laminated core structure, the fields near the air gap were evaluated. To test the impact of gap length on the fringing flux-induced eddy current losses, the air gap was set to three different sizes (0.25 mm, 0.5 mm, and 1 mm) at a fixed frequency of 25 kHz and flux density of 0.1 T. A field overlay of ohmic loss was created for these gapped models, displaying only the eddy current losses inducing by the fringing flux. The field plots for eddy current loss in the core with the different gaps are shown in Figure 10. As suggested by the gap loss model for nanocrystalline cores [28], the eddy current losses increase with the size of the air gap.

What is not clear from these simulations is how these eddy current losses scale with gap length. By conducting a series of experiments in Section 4, core loss data will be collected and compared to the gap loss model to better quantify the impact of gap length on gap losses.

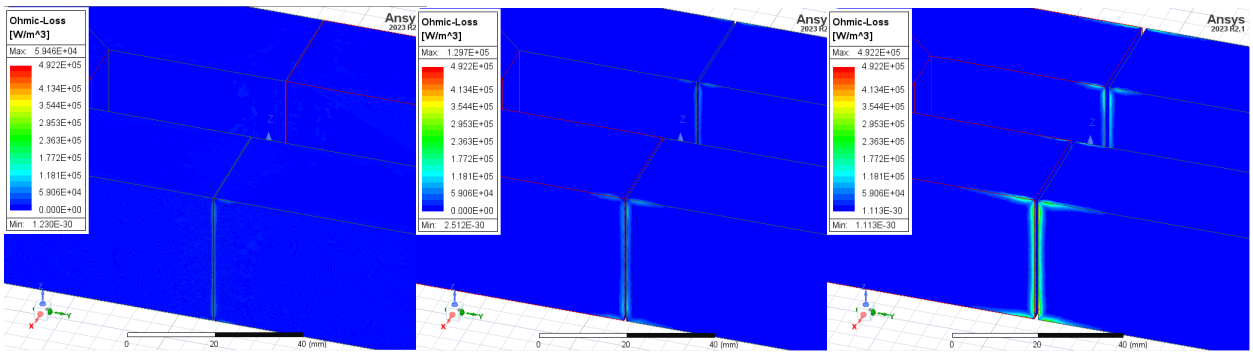

Figure 10: Ohmic Loss Distribution at 25 kHz, 0.1 T with 0.25mm, 0.5mm, and 1mm Gaps

4.0 Experiments

The following section details the experiments performed to measure losses in the core of a test inductor with a series of discrete air gap sizes. The primary goals of this experimental work are to observe the impact of increasing gap length on the losses of a laminated, nanocrystalline core and to evaluate the ability of the fringing gap loss model to predict these additional losses.

4.1 Measurement Method

There are multiple approaches to measuring power loss in magnetic cores. It can be obtained directly by measuring the electrical power lost in the core or by measuring the heat dissipated in the core through a calorimetric approach. These approaches have varying levels of accuracy, and often come with the challenge of separating winding losses from total power loss measurements [24]. Instead of directly measuring the electrical and thermal energy lost in the inductor, core loss can be obtained by measuring the core's flux density, B, and magnetic field strength, H. The area of the B-H loop, or the curve relating the two quantities, is proportional to the power loss per cycle [6].

The selected method for core loss measurement is known as the two-winding method. A conceptual diagram of the setup is pictured in Figure 11 . The primary winding in this setup is excited with current, generating flux in the core. The leads of the secondary winding are left open, so that the voltage induced across it by the core flux can be measured. Using Ampere's Law, the inductor's mean magnetic path length l_m, primary current i_p, and number of primary winding turns N_p, can calculate the magnetic field strength. Similarly, Faraday's Law allows the flux density to be calculated from the voltage induced on the secondary winding v_s, secondary winding turns N_s, and core cross-sectional area A_e [17]. The time-varying equations for H and B are shown in (4.1) and (4.2), respectively.

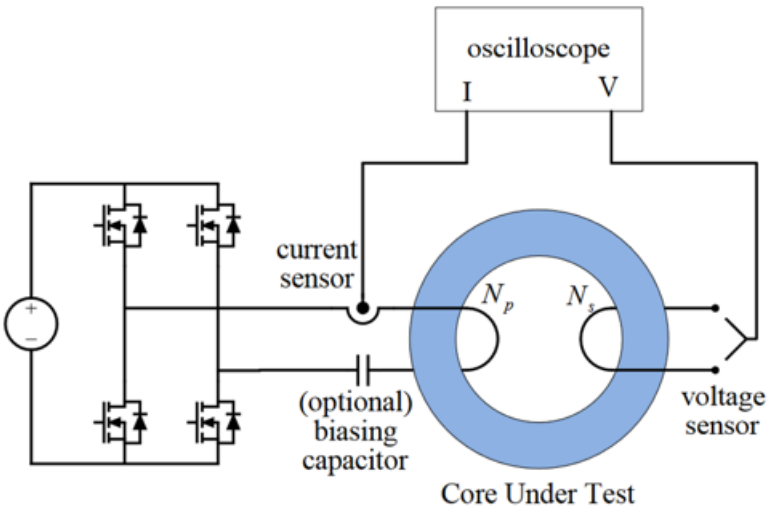

Figure 11: Conceptual Diagram of Two-Winding Core Loss Measurement Setup [17]

$$H(t) = \frac{N_p i_p(t)}{l_m} \tag{4.1}$$

$$B(t) = \frac{1}{N_s A_e} \int_0^T v_s(\tau) d\tau \tag{4.2}$$

4.2 Core Under Test

A cut Finemet FT-3TL core sample was selected for this experiment. This core consists of several, 17 micrometer-thick sheets, separated by layers of epoxy resin. The core is pictured along with a diagram labeling the core's dimensions in Figure 12 [2]. The dimensions of the core are listed in Table 5, corresponding to the labels Figure 12. A vice was used to hold the core halves together and sheets of insulation paper of varying thickness were used to maintain spacing between them for the gapped core configurations.

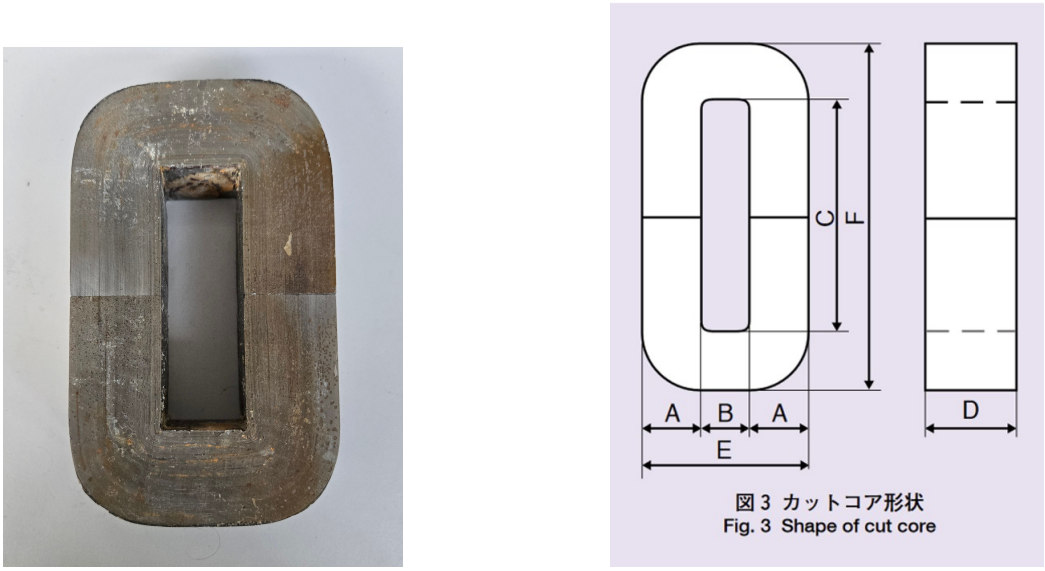

Figure 12: Core Under Test (left) and Diagram of Core Dimensions (right) [2]

Table 5: Dimensions of Core Under Test

Dimension	**Length (mm)**
A	27.5
B	25
C	84.2
D	33
E	80
F	139.2

The core was fitted with two windings for this experiment: a six-turn primary excitation winding used to generate magnetic flux in the core, and a six-turn secondary sensing winding used to measure the core flux. The primary winding, composed of three parallel bundles of Litz wire, was placed around the vertical legs of the core. Litz wire uses several smaller, individually insulated wires to make a single conductor bundle. These individual wires have a radius less than one skin depth of the conductor material. Since the focus of the study

is core loss, Litz wire was selected to mitigate the AC winding effects discussed in Section 1 [13]. To minimize potential leakage flux and evenly distribute flux in the core, a pair of bobbins was used to evenly divide and center the turns around each gap. The secondary winding, using magnet wire, was placed around the top half of the core.

4.3 Current Amplifier Setup

The leads of the primary winding were connected to the output of a Keysight 33500B Waveform Generator and AE Techron 7224 RF Amplifier. This setup was used to excite the winding with sinusoidal currents at selected frequencies, with a 1 mF DC-blocking capacitor. A 30 Amp Teledyne-Lecroy current probe was used to measure current in the primary winding. Two Teledyne-Lecroy HVB3220 2 kV differential probes were placed across both windings to measure voltage across the inductor and voltage induced on the secondary winding. The current and voltage signals of interest were recorded using both a Teledyne-Lecroy 3104Z Oscilloscope and a Yokogawa WT5000 Power Analyzer. The complete test setup is pictured in Figure 13.

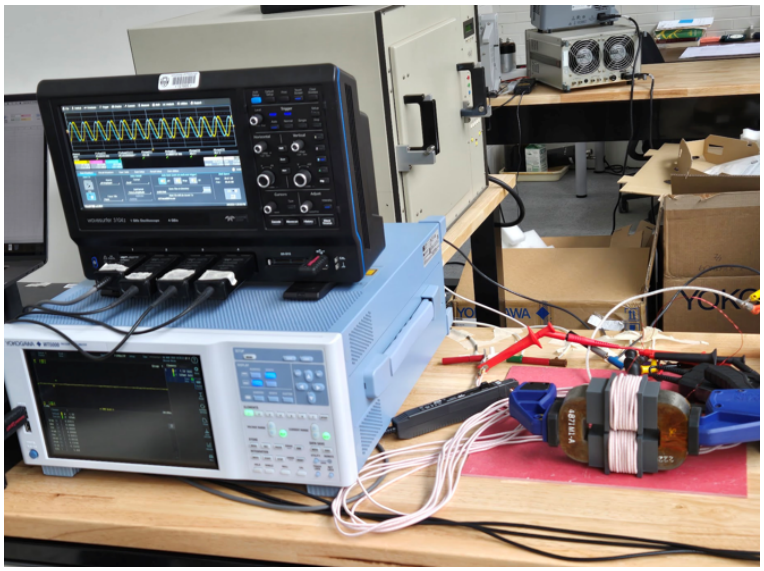

Figure 13: Core Loss Measurement Testbed

4.4 Experimental Procedure

Since core losses are directly related to the frequency of the time-varying fields and magnitude of flux density, the tests were conducted at five frequencies (1 kHz, 5 kHz, 10 kHz, 25 kHz, and 50 kHz), and four target flux densities (0.03 T, 0.05 T, 0.07 T, 0.1 T). To validate the setup and measure the impact of gap length on core loss, a baseline of loss values must be established. This test is conducted by measuring core losses when the cut core halves are pressed together with no gap spacing, or at the "minimum gap" case. This assumes that the fringing flux path has been minimized, and that the only core loss contributions being measured are the magnetizing loss and direct gap loss. By incrementing the gap size from the minimum gap case and repeating the loss measurements at the target frequencies and flux densities, the fringing gap loss can be measured.

For each measurement, the waveform generator was set to the desired frequency and was turned on, exciting the core with a weak flux excitation. To avoid overloading the amplifier, the current is slowly increased until the desired flux density is reached. The root mean square (RMS) value of the secondary winding voltage measured on the power analyzer and oscilloscope were used to monitor the flux density in the core. Before each round of tests was conducted, the RMS voltages corresponding to each target flux density were calculated using (4.3), derived from (4.2) [15]. When the secondary voltage corresponding to the target flux density is reached, the waveforms from the power analyzer and oscilloscope are saved. The power analyzer measurements of i_p and V_s are shown in Figure 14.

$$V_{s,rms} = 4.44 B_m N_s A_e f \tag{4.3}$$

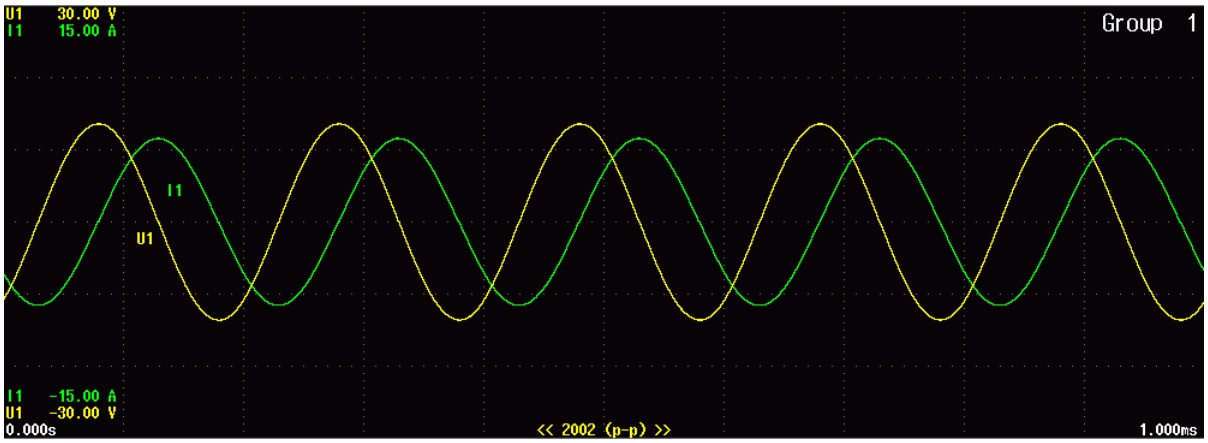

Figure 14: Power Analyzer Measurements of Primary Current and Secondary Voltage

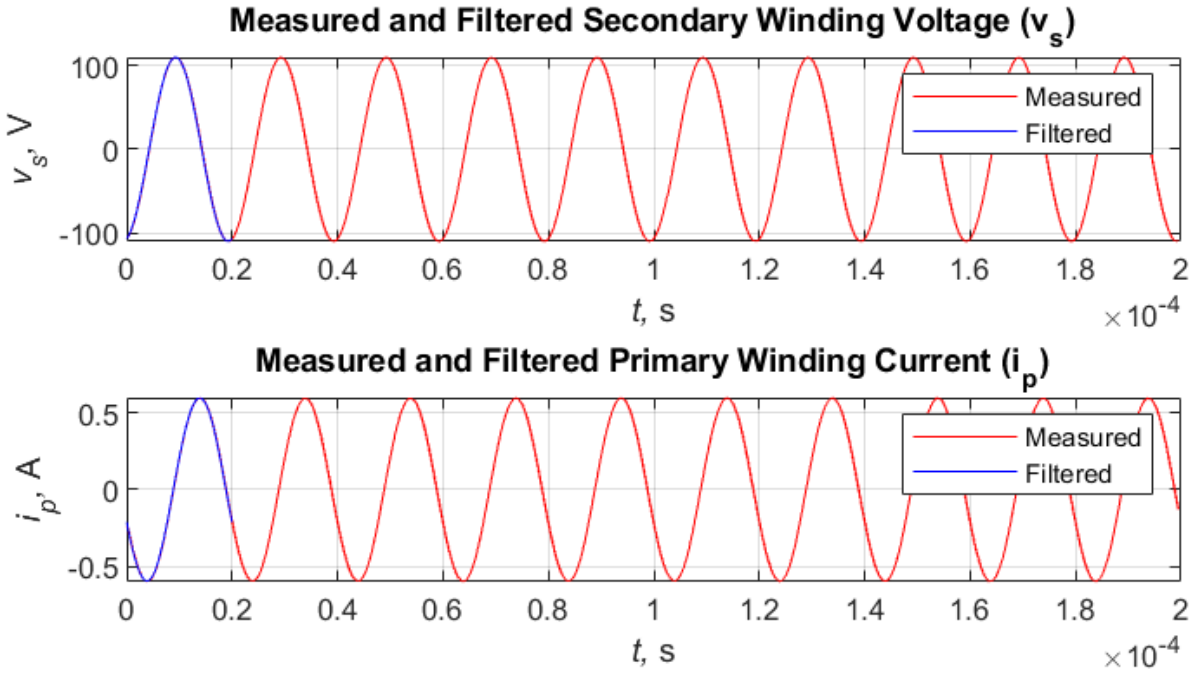

Figure 15: Measured vs. Filtered Signals in Matlab

Using least-squares fitting, Fourier series coefficients were fit to the measured signals to filter any noise from the measured signals. Then, the waveforms were reconstructed over one period using the resulting coefficients. By sampling a single period of the primary current and

secondary voltage waveforms and using (4.2) and (4.1), the B and H signals were created, allowing the construction of the B-H loops for each test case. A group of B-H loops for a specific gap length and frequency are pictured in Figure 16. By calculating the area of these loops, the core losses of the sample were obtained.

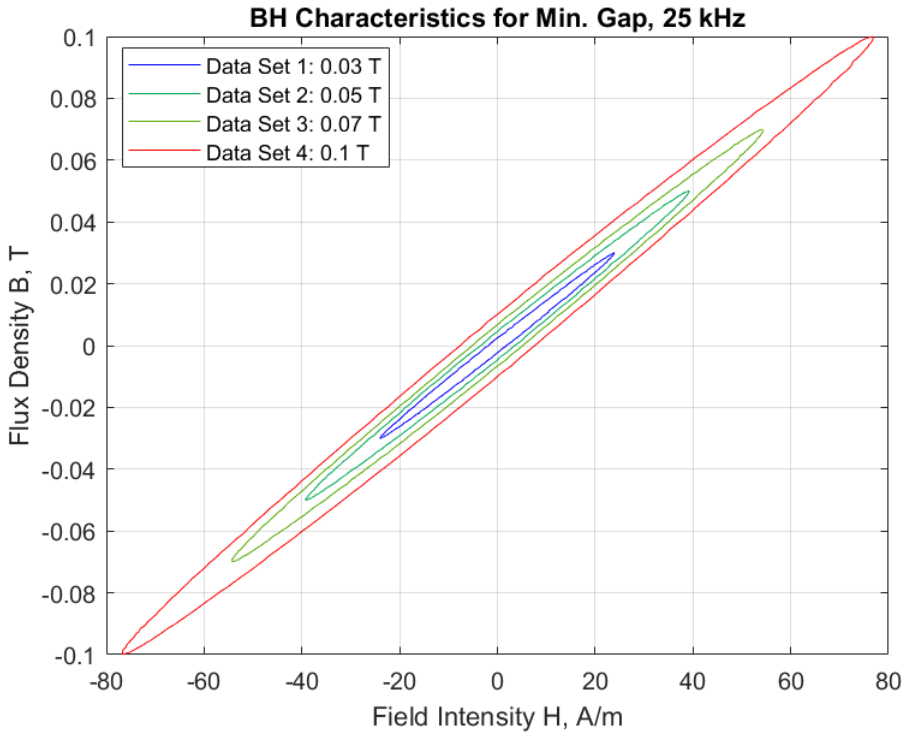

Figure 16: B-H Loops Measured from Core with Minimum Gap at 25 kHz

4.5 Minimum Gap Baseline Measurements

The goal of the experiment is to observe, for a fixed frequency and flux density, the increases in core loss as the air gap is increased. To measure the increase in loss, a reliable set of baseline loss measurements must be taken before the discrete air gap is introduced. This baseline was obtained by measuring the core's losses with minimum gap, or with a vice holding the core halves together and no spacing between them. Since the fringing flux

paths are minimized in this configuration, the measured losses were expected be close to those predicted by the Steinmetz Equation, using the documented coefficients. Figure 17 compares the measured core loss values with those calculated using the Steinmetz Equation and the documented coefficients for the core under test.

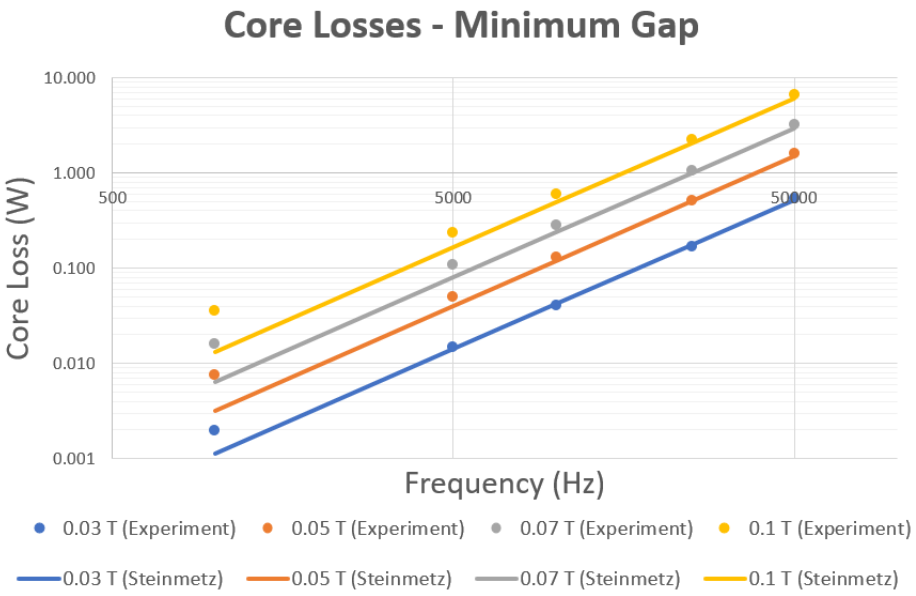

Figure 17: Measured Minimum Gap Core Losses vs. Steinmetz Predictions

The experimentally measured core losses show significant agreement with the Steinmetz predictions at the higher frequencies tested. At 10 kHz and higher, most of the losses measured are within 20% of the expected Steinmetz losses. Below 10 kHz, the core losses predicted by the Steinmetz equation underestimate the experimentally measured losses. At the 1 kHz test cases, the measured losses were two to three times higher than predicted, resulting in errors between 100% and 200%.

From (4.3), it is known that at a higher frequency, a larger induced voltage V_s is needed to reach the same target flux density. To reach this larger induced voltage, more current is needed to excite the primary winding. Therefore, the tests performed at lower frequencies are operating at lower power levels. This may cause any deviations on the scale of mW present in the setup to become apparent at these lower frequencies.

To more rigorously evaluate the quality of these baseline measurements, the data was fit to the same structure as the Steinmetz Equation: a power function of both frequency and flux density. The resulting coefficients were then compared to the documented Steinmetz coefficients, listed in Table 6. The coefficients for frequency and flux density are very close, supporting the assumption that minimizing the gap length also minimizes the contribution of gap loss.

Table 6: Comparison of Steinmetz Coefficients

Coefficient	**Documented**	**Fit**
k (W/kg)	1.663e-05	3.673e-05
α	1.570	1.558
β	2.043	2.058

4.6 Gap Loss Measurements

The air gap between the core halves was gradually increased and the tests were repeated at gap lengths of 0.127 mm, 0.254 mm, 0.508 mm, and 1.016 mm. Using the same number of turns for the primary and secondary windings allowed the use of the same target V_s values as indicators of flux density. Since adding the air gap increases the reluctance of the inductor, higher currents were needed to excite the core and achieve these target secondary voltages and flux densities. For the 0.508 mm and 1.016 mm gaps at 50 kHz, the current amplifier was unable to supply enough current to reach 0.1 T, the highest flux density target. Instead, the highest values attainable at 50 kHz were recorded: 0.09 T for the 0.508mm gap and 0.08 T for the 1.016 mm gap. To calculate gap loss for those test cases, the core loss was also measured with minimum gap at the same frequency and flux densities.

The gap losses must be estimated using the collected core loss data, as it cannot be directly measured. At the minimum gap case, the cut core halves will always have a small, nonzero gap between them, meaning that there will still be some fringing gap loss that cannot

be separated from the total core loss measurements. From the baseline measurements, these minimum gap losses are very close to the magnetizing losses predicted by the Steinmetz Equation. For this reason, it is assumed that the fringing gap loss P_{gap} is the difference between the core loss P_c measured with gap length l_g and core loss measured with the minimum gap $l_{g_{min}}$, taken at the same frequency f and flux density B_m:

$$P_{gap}(l_g, f, B_m) = P_c(l_g, f, B_m) - P_c(l_{g_{min}}, f, B_m) \tag{4.4}$$

After all tests were performed, the gap losses were calculated using (4.4) and compared to the values predicted by the fringing gap loss model in (2.7). Figure 18, Figure 19, and Figure 20 are plots of the gap losses in response to changing frequency, peak flux density, and gap length. The dashed lines in the plots represent predicted values that are not accompanied by a corresponding measured value, as target flux density could not be reached for those test cases.

The gap loss increases nearly linearly with gap length, in line with the relationship predicted by the model. Similarly, the gap loss increases in response to increasing flux density. However, the measured gap losses show lower sensitivity to frequency than the predicted values from the model. Like the minimum gap core loss measurements, the gap losses are consistently larger than the gap loss model predictions at 5 kHz and lower.

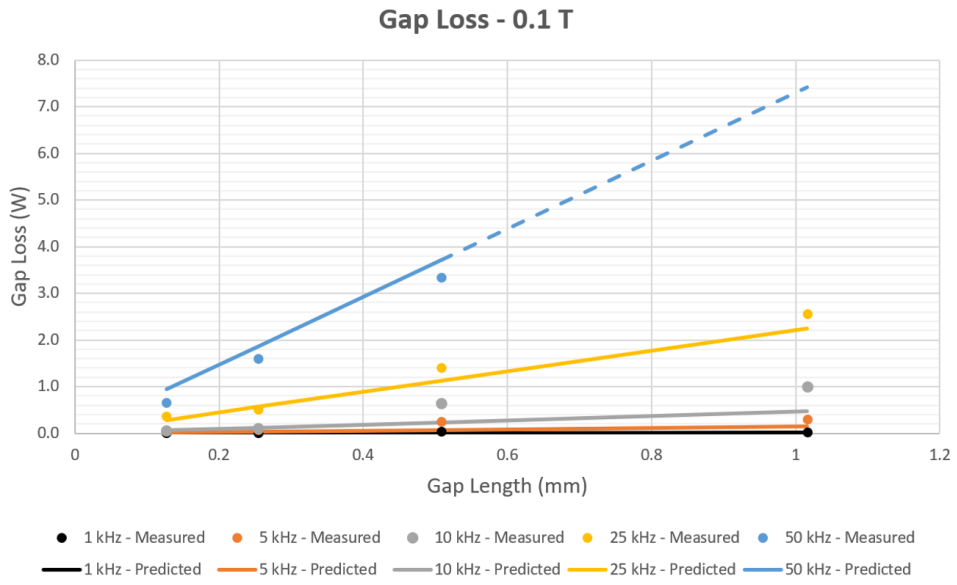

Figure 18: Plot of Gap Loss vs. Gap Length

Figure 19: Plot of Gap Loss vs. Flux Density

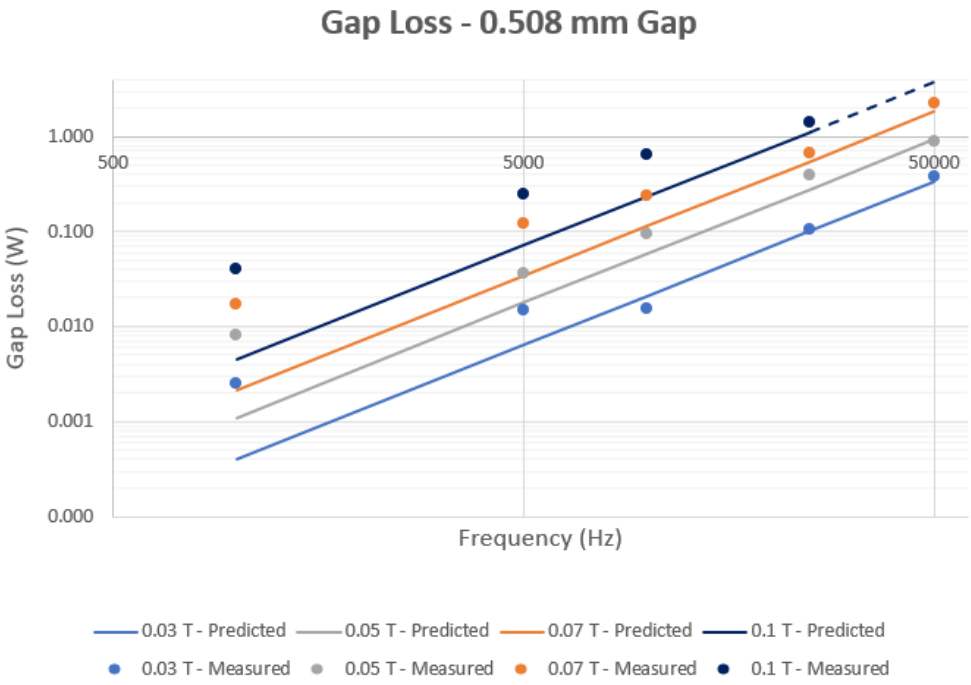

Figure 20: Plot of Gap Loss vs. Frequency

To quantify the relationships between gap loss and the independent variables, the data was fit to a model using nonlinear least-squares regression [12]. The model format selected is similar to (2.7) [28], where gap loss is a power function of lamination width, gap length, frequency, and peak flux density. Lamination width remained constant at 33 mm throughout this experiment as only one core was used, so the $D^{1.65}$ term was not changed. The resulting power coefficients for gap length k_{l_g}, frequency k_f, and peak flux density k_{B_m} were 0.9013, 1.2206, and 2.1094, respectively. The numerical constant, k_g, was determined to be 0.3896. These coefficients result in (4.5), an equation to calculate gap loss in a cut Finemet core.

Both the coefficients fit to the experimental data and the coefficients from the model proposed by Wang in (2.7) [28] are listed in Table 7. The fit coefficients for the gap length and peak flux density terms are close to those used in the gap loss model, aligning with behavior observed in Figure 18 and Figure 19. The coefficients fit from the measured data yielded a significantly lower coefficient for frequency, corresponding to lower accuracy observed at 1 kHz and 5 kHz. This could be related to the deviations between measured and predicted

values observed in the measurements taken at lower frequencies, since the magnitude of the loss is lower than those measured above 10 kHz. Also, this could be a result of applying the fringing gap loss model to lower frequencies than those simulated by Wang et al. in [28]. The model was developed using losses simulated from 40 kHz to 200 kHz, while the experiments measured losses between 1 kHz and 50 kHz. Table 7 also lists the ranges of gap lengths and flux densities considered in the simulations in [28] and the experiments detailed in this section.

$$P_{gap}(l_g, f, B_m, D) = 0.3896 {l_g}^{0.9013} f^{1.2206} {B_m}^{2.1094} D^{1.65} \tag{4.5}$$

Table 7: Comparison of Coefficients for Gap Loss Model and Fit to Experimental Data

	Wang's Model		*Experimental Fit*	
Coefficient	**Value**	**Tested Range**	**Value**	**Tested Range**
k_g	1.68e-3	N/A	1.4e-3	N/A
k_{l_g}	1	1 - 2.6 mm	0.9013	0.127 - 1.016 mm
k_f	1.72	40 - 200 kHz	1.2206	1 - 50 kHz
k_{B_m}	2	0.1 - 0.2 T	2.1094	0.03 - 0.1 T

5.0 Multi-Objective Optimization

Now that the relationship between gap size and nanocrystalline core loss has been evaluated through simulation and experiments, the impact of these gap losses on the inductor design process is explored. The selected gap losses were integrated into a genetic algorithm-based multi-objective optimization tool in MATLAB. Originally developed for UI-core DC inductors, the code was modified for UU-core inductors [23]. The impact of these additional losses on both the individual designs and the tradeoff point between nanocrystalline and ferrite core materials are explored in this chapter.

5.1 Genetic Algorithm

A genetic algorithm is used to perform the multi-objective optimization work described in this chapter. Based on the biological concept of natural selection, this algorithm operates on populations of separate designs. Each design has a set of genes, with each one corresponding to a characteristic that is used to calculate the design's key metrics and fitness. Operations are performed on each population: selecting elite designs, "mating" to combine characteristics of selected designs, and randomly "mutating" designs to introduce further changes to the population. A fitness function is used to evaluate each member of a population, influencing which characteristics will persist into later iterations, or generations.

Several aspects of this process separate the genetic algorithm from traditional optimization algorithms. Many optimization algorithms only operate on a single design with each iteration, not an entire population. The genetic algorithm also employs probabilistic operations in its optimization, as opposed to deterministic operations used in traditional algorithms [23].

5.2 Multi-Objective Design Process

Regardless of the algorithm used, multi-objective optimization follows a set process consisting of the following steps: identifying the search space, defining design constraints, formulation of design metrics, and synthesis of a fitness function [23]. The design space refers to the variables the optimization is changing to optimize the fitness of designs created. In the case of the UU-core inductors being optimized, this refers to the core material and the physical dimensions of both the core and winding. The goal of this optimization is to create designs satisfying the requirements set forth by the application, while minimizing the key metrics of mass and power loss.

5.3 Design Space and Constraints

This section details the free parameters that make up the design space, along with the assumptions and constraints used to evaluate the generated designs. Most of the free parameters pertain to the dimensions of the inductor core and winding, listed in Table 8. These parameters not only impact the physical footprint of the designs, but other properties including inductance, flux density, current density, and temperature rise.

The materials in the design space are limited to nanocrystalline and MnZn ferrite cores and copper conductors. The nanocrystalline core definition used permeability data for Finemet FT-3M and the Steinmetz coefficients for a cut sample of Finemet core used in Section 3 and Section 4. This core loss data was selected because the designs being generated are gapped, meaning their losses would likely resemble that of a cut core. The ferrite core definition was assigned permeability data for MN67 [23] and the core loss data used by Neumayr in [18]. These material selections are consistent with the properties of the magentic materials outlined in Section 1, allowing evaluation of the impact gap loss has on the general fitness of each class of core material.

To minimize the impact of AC winding losses and keep the winding loss contributions consistent, the designs are limited to copper Litz wire conductors and the loss due to skin and proximity effects are neglected. Since the diameter of a Litz wire bundle is larger than that of a solid conductor with equivalent cross-sectional area, an additional packing factor is applied to the conductor diameter [27].

Table 8: Free Parameters for Optimization

Parameter	**Description**	**Min. Value**	**Max Value**
T_{cr}	Type of core material	1 (Ferrite)	2 (Nanocrystalline)
g	Gap length (mm)	0.1	10
l_c	Length of core (mm)	10	100
w_e	U-core end width (mm)	10	1e3
a_c	Cross-sectional conductor area (m^2)	1	1e4
N_w	Desired slot width in conductors	1	1e3
N_d	Desired slot depth in conductors	1	1
c_w	Slot clearance in width (mm)	1	100
c_d	Slot clearance in depth (mm)	1	100

Several constraints have been implemented to evaluate the designs. Many of the constraints regulate the physical dimensions of the design: the number of winding turns, conductor packing factor, conductor current density, and the inductor aspect ratio. This eliminates designs that may satisfy the design requirements but have undesirable qualities such as overheating conductors and impractical shapes [23].

Other constraints are concerned with the magnetic and thermal properties of the inductor designs. These constraints eliminate designs that do not meet the required inductance, approach saturation flux density (>80% B_{sat}), and have excessive temperature rise (>60° C). The final constraints used to bound the search space are the maximum values allowed on the key metrics for optimization, mass (20 kg) and loss (500 W). While the goal of these

constraints is to bound the design space, the maximum mass and loss values were selected to allow trends among the optimal designs to be clearly visible. More strict limits will be selected after the initial analysis is completed to perform a more focused comparison between specific designs.

5.4 Impact of Gap Loss on Optimal Designs

The chosen application for the multi-objective optimization was a 12 μH DC filter inductor operating at 50 kHz with 110 A of DC current and 56 A current ripple. The optimization was run for 1000 generations with populations of 1000 designs. After performing the optimization, pareto optimal fronts were created. These are plots of the optimal designs in the space, organized by their respective mass and loss values. This optimal group of designs are nondominated, meaning that no single design in the design space will offer both lower mass and lower loss [23]. Unless one metric is expressly preferred over another by the design application, identifying the "knee", or bend, in the pareto front will provide designs with the best balance between the two metrics [8].

The optimization was run with only the winding loss and magnetizing core loss being considered for designs, the latter calculated using the Steinmetz Equation and each core material's respective coefficients. The goal of these optimizations is to observe what metrics the knee of the pareto optimal front falls near when gap losses are neglected. Though all designs in the pareto optimal front are "optimal", an efficient design that is very heavy and a light design with excessive loss are less likely to be selected [23]. The initial pareto optimal front of inductor designs are shown in Figure 21. Designs using nanocrystalline cores are marked in blue, while ferrite core inductors are marked in red.

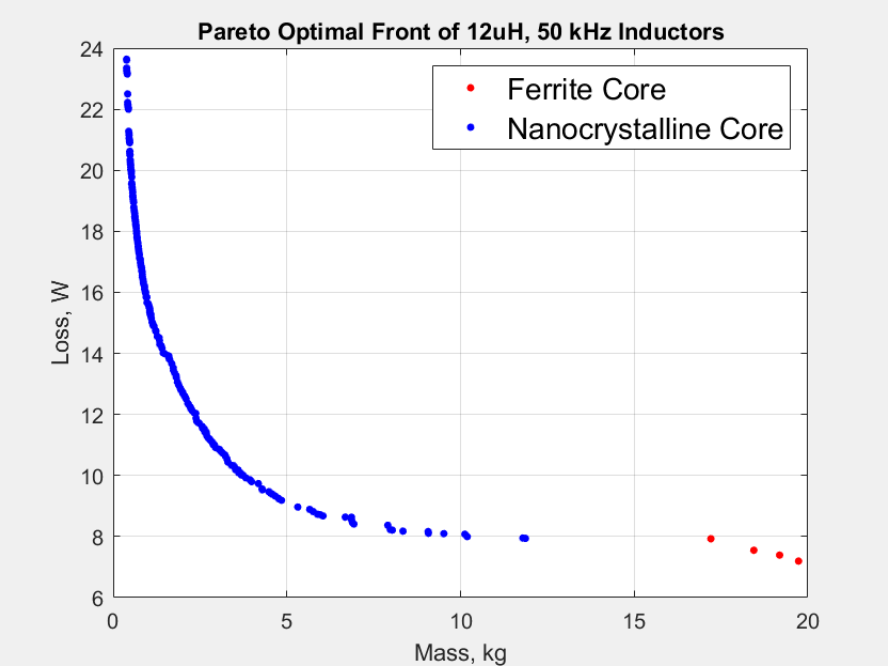

Figure 21: Pareto Optimal Front of Inductor Designs Without Gap Loss

The pareto optimal front for 12 uH, 50 kHz inductors is dominated by designs with nanocrystalline cores, with the knee occuring near 11 W and 3 kg. A few ferrite core designs offer incremental improvements in losses under 8 W, but this comes at the expense of masses approaching 20 kg. For the 50 kHz frequency, the inductors created using nanocrystalline cores offer a better balance between mass and loss than the ferrite cores.

Since the inductor designs being optimized are gapped, it is important to understand the impacts that gap loss will have on the ability to minimize the mass and loss of these designs. After optimizing designs with respect to only magnetizing core loss, the optimization was repeated with gap loss models integrated into the framework. As discussed in Section 2, the mechanisms contributing to gap loss differ between nanocrystalline and ferrite cores. The fringing gap loss model in (4.4) is used for nanocrystalline core designs and the surface loss equation in (2.6) is used for MnZn ferrite designs [28, 18]. The pareto optimal front generated with the gap loss models included is shown in Figure 22.

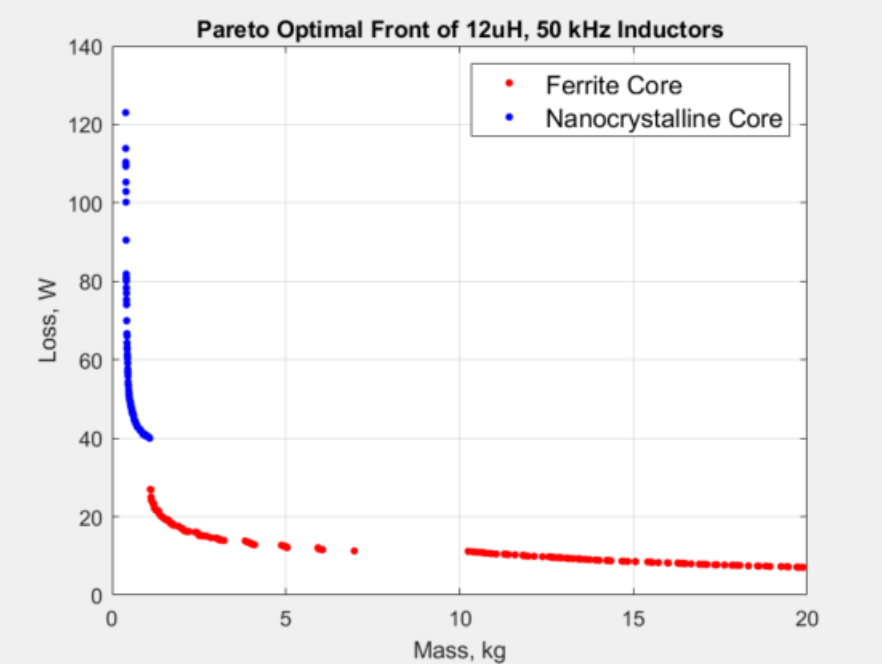

Figure 22: Pareto Optimal Front of Inductor Designs With Gap Loss

The introduction of gap loss has a clear impact on the optimized designs. The nanocrystalline cores still offer the most lightweight designs, but the total losses have increased significantly. The nanocrystalline designs closest to the knee of the curve have losses well above 40 W, approximately four to five times more than the designs created neglecting gap loss. The pareto optimal front now includes more ferrite core designs, offering lower loss than the nanocrystalline designs for masses above 1 kg. The ferrite designs near the knee have losses between 15 W and 30 W, which is significantly lower than that of nanocrystalline designs with similar mass. Regardless, none of the designs seem to be capable of providing the metrics observed in the optimization performed without gap loss. While nanocrystalline cores initially appeared to be the optimal core material for the 12 μH inductor designs at 50 kHz, the introduction of gap loss models suggests that both nanocrystalline and ferrite cores both provide competitive designs for this application. If smaller mass is strongly preferred, nanocrystalline cores are likely the best option. Alternatively, ferrite cores are best if the primary objective is to have as little loss as possible.

5.5 Design Comparison and Tradeoff Frequencies

After gap losses were added to the optimization, the overall fitness of the designs decreased, evidenced by the changes observed in the pareto optimal front. Operating frequency is a key factor in deciding which magnetic core material should be used, so it is often useful to know the tradeoff point between materials. To identify the frequency ranges where a tradeoff between nanocrystalline and ferrite designs occur for the 12 μH DC filter inductor application, the optimizations were repeated at frequencies of 10 kHz and 100 kHz. The resulting pareto optimal fronts are shown in Figure 23 and Figure 24.

When gap loss is neglected, nanocrystalline cores offer better balance between mass and loss at all selected frequencies. At 100 kHz, ferrite designs make up a larger portion of the pareto optimal front, suggesting that the designs are nearing a tradeoff point. However, these ferrite designs still have large masses over 10 kg, twice the mass of nanocrystalline designs with similar loss. With the gap loss model integrated, the total losses of nanocrystalline designs increase significantly at all frequencies. While direct gap loss is being calculated for ferrite designs, the magnitude of these losses are much lower than the fringing gap losses, which quickly become a dominant loss contribution in nanocrystalline inductor designs.

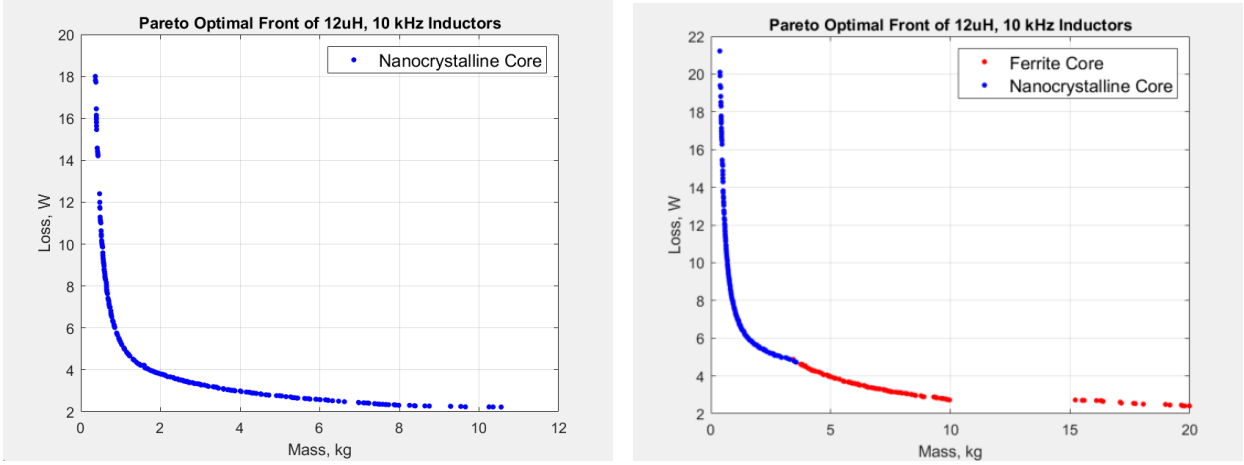

Figure 23: 10 kHz Pareto Fronts Without (left) and With (right) Gap Loss

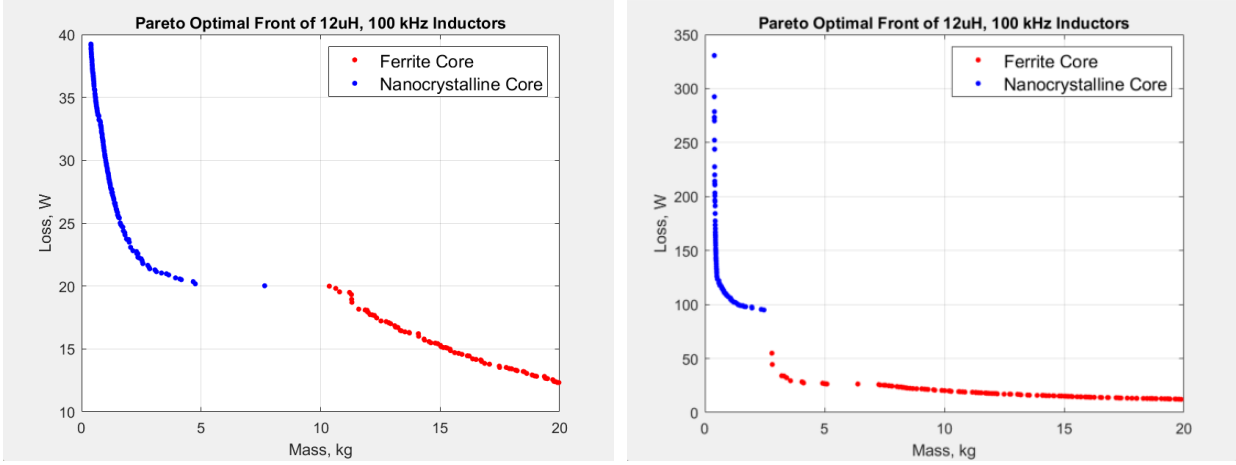

Figure 24: 100 kHz Pareto Fronts Without (left) and With (right) Gap Loss

To better visualize the relationship between frequency and the fitness of core materials, one design of each material was selected from each optimization. A maximum allowable mass was imposed, and designs closest to this value were selected. For the optimizations without gap loss, this maximum mass was 2.5 kg. The knee of the pareto fronts shift along the x-axis toward higher mass values as frequency increases, resulting in a threshold of 5 kg being used for the optimizations including gap loss models. Once selected, the losses of the designs were plotted against frequency, shown in Figure 25.

These plots align with the trends indicated in the pareto optimal fronts. For gapped inductors, neglecting gap loss would incorrectly suggest that nanocrystalline cores are the optimal core material up to 100 kHz, with a possible tradeoff occuring beyond that. This tradeoff point drops to the 10-50 kHz range when gap losses are accounted for, since the losses in nanocrystalline designs can become an order of magnitude larger than those in the ferrite designs at 100 kHz.

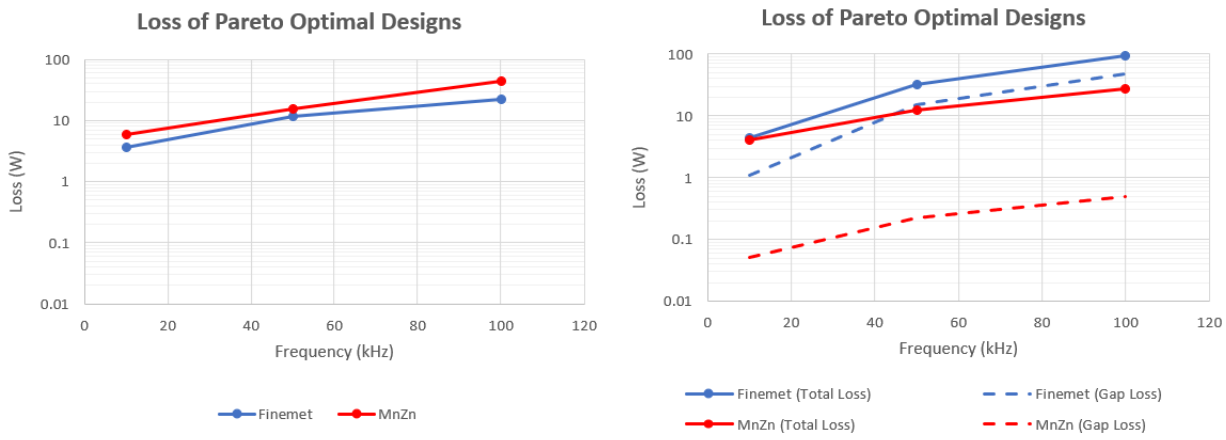

Figure 25: Comparison of Designs Without (left) and With (right) Gap Loss

5.6 Nanocrystalline Inductor Design Trends

The optimization work has shown that the inclusion of air gaps has the most significant impact on the designs using nanocrystalline inductor cores, in many instances increasing the total losses by an order of magnitude. In addition to locating the tradeoff frequencies betwen nanocrystalline and ferrite cores, it is also important to identify trends in designs that have been optimized with the gap loss models. Since the goal of the optimization is to minimize mass and loss, cores will be designed in ways that naturally minimize gap loss.

Ten nanocrystalline designs were selected from the 12 μH, 50 kHz pareto optimal fronts: five selected from the designs generated before gap loss models were integrated and five selected after. The intention was to select designs near the knee of the pareto front with high fitness values for both metrics. The fitness values for both the mass and loss of the pareto front designs were normalized. Then, the two normalized fitness values were multiplied to

give the designs a third fitness value. The designs were sorted by this combined fitness value, and the those with the five highest values were selected for evaluation. The geometries of the optimal designs are pictured in Figure 26, and dimensions of the cores and conductors are compared in Table 9.

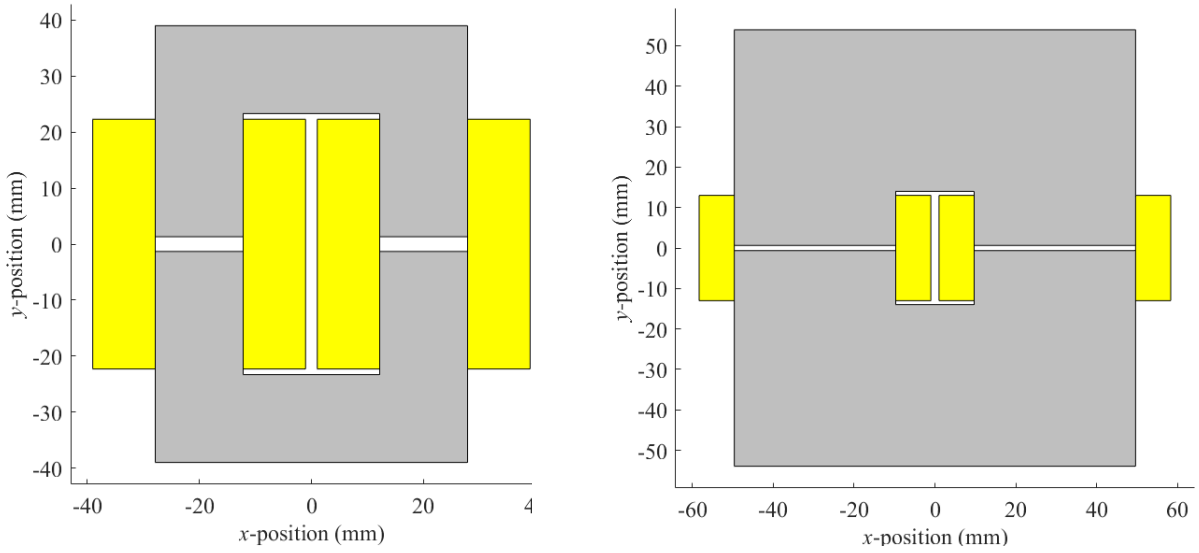

Figure 26: Optimal Nanocrystalline Designs Without (left) and With Gap Loss (right)

Table 9: Core and Winding Dimensions of Selected Nanocrystalline Inductor Designs

Parameter	**Description**	**No Gap Loss**	**Gap Loss**
g	Gap length (mm)	2.22	1.29
l_c	Lamination Width (mm)	32.13	13.43
w_e	U-core end width (mm)	13.43	39.93
A_e	Core cross-sectional area (mm^2)	345.12	429.05
a_c	Conductor cross-sectional area (mm^2)	31.65	52.50

After the gap loss model was integrated into the optimization framework, the selected designs near the knee consistently had smaller gap lengths and core lengths. The core length, l_c, refers to the core's size along the z-axis, directly corresponding to the nanocrystalline

ribbon width. The fringing gap loss model increases with both gap length and ribbon width, terms l_g and D in (7), so these trends are to be expected. Conversely, these designs tend to have larger core widths w_e, impacting size along the x-axis. This appears to be a response to the decreasing l_c values, as the cross-sectional area A_e, the product of l_c and w_e, remains similar across all ten designs. The increased core width leads to a much smaller core window, reducing the area available for conductors. As a result, many of the designs created with gap loss have fewer conductor turns.

These trends suggest that using shorter gap lengths and narrower ribbons are ways to mitigate fringing gap losses in nanocrystalline inductor designs. The optimization tending toward these smaller ribbon widths aligns with the work conducted by Calderon-Lopez et al. in [7], which stacked multiple cores with smaller ribbon width to reduce the continuous surface area for the fringing flux-induced eddy currents to form.

6.0 Conclusion

Placing air gaps in magnetic cores is a common technique in the design of magnetic components, but often comes at the cost of increased power losses. This work explores the mechanisms contributing to these gap losses through a combination of finite-element modeling and experimental measurements. By measuring the losses of a cut Finemet inductor core over a range of increasing gap lengths, an existing gap loss model is evaluated. The measured gap losses align with the trends suggested by the model, specifically the dependence on gap length. As gap lengths reach 1 mm and frequencies reach 50 kHz, the measured core losses can increase to almost twice those predicted by the commonly used Steinmetz Equation, showing that accurate predictions of gap loss are needed to design gapped inductors.

The multi-objective optimization provides further insight on the impact of gap losses. For a selected DC filter inductor application, the gap losses become dominant in designs using nanocrystalline cores, often making up more than half the total inductor losses. Optimization was also used to compare inductors with nanocrystalline cores to those with ferrite cores. If only the Steinmetz Equation is used to predict core losses, nanocrystalline cores appear to be the optimal core material for this application up to 100 kHz. When accounting for gap losses, ferrite core designs become more attractive near 50 kHz due to their lower losses, but still cannot achieve the the lower mass that nanocrystalline designs offer. While the high permeability and mass density of nanocrystalline cores make them suitable for use in power magnetic components, accurately predicting losses is critical to reaching the efficiency and power density goals needed to drive EV development.

This work can be expanded by testing cores over wider ranges of frequencies and flux densities, allowing better characterization of these gap losses for high frequency and high power applications. Developing the optimization framework to consider the impact of fringing gap flux on winding losses would allow a greater understanding of the impacts of air gaps on magnetic component designs.

Bibliography

[1] Electrical and electronics technical team roadmap roadmap, 10 2017.

[2] Finemet f3cc series cut core, 5 2017.

[3] Igbt sic gate driver fundamentals: Enabling the world to do more with less power, 2021.

[4] Malcolm Baumann. A simple analytical method to calculate air gap induced eddy current losses in inductive components, 3 2018.

[5] G. Bertotti. General properties of power losses in soft ferromagnetic materials. *IEEE Transactions on Magnetics*, 24(1):621–630, 1988.

[6] Chris Bracken, Richard Beddingfield, Mark A. Juds, Bharadwaj Reddy Andapally, Brandon Grainger, and Paul R. Ohodnicki. Standardization of Core and Component Characterization at the Advanced Magnetics for Power and Energy Development Laboratory. In *2023 IEEE Transportation Electrification Conference and Expo, ITEC 2023*. Institute of Electrical and Electronics Engineers Inc., 2023.

[7] Gerardo Calderon-Lopez, Yiren Wang, and Andrew J. Forsyth. Mitigation of Gap Losses in Nanocrystalline Tape-Wound Cores. *IEEE Transactions on Power Electronics*, 34(5):4656–4664, May 2019. Publisher: Institute of Electrical and Electronics Engineers Inc.

[8] Oliver Cuate and Oliver Schütze. Pareto explorer for finding the knee for many objective optimization problems. *Mathematics*, 8, 2020.

[9] Hirotoshi Fukunaga, Tohru Eguchi, Yukihiko Ohta, and Hidenori Kakehashi. Core loss in amorphous cut cores with air gaps. *IEEE Transactions on Magnetics*, 25:2694–2698, 1989.

[10] Roderick A. Gomez, Shamar F. Christian, German G. Oggier, Roberto A. Fantino, Juan C. Balda, and Yue Zhao. Etching process to reduce interlamination short circuits and core loss comparison for tape-wound cut cores. Institute of Electrical and Electronics Engineers Inc., 2022.

[11] Roderick A. Gomez, David A. Porras Fernandez, German G. Oggier, Juan C. Balda, and Yue Zhao. Comparison of High-Frequency Ferrite and Nanocrystalline Core Losses Using Identical Geometries. In *2022 IEEE 13th International Symposium on Power Electronics for Distributed Generation Systems, PEDG 2022*. Institute of Electrical and Electronics Engineers Inc., 2022.

[12] The MathWorks Inc. Statistics and machine learning toolbox, 2022.

[13] Kyle Jensen. Litz wire: Practical design considerations for today's high frequency applications, 2020.

[14] Radoslaw Jez. Influence of the distributed air gap on the parameters of an industrial inductor. *IEEE Transactions on Magnetics*, 53, 11 2017.

[15] Dave Levasseur. Why 4.44?, 1998.

[16] Jingsong Li, Qingxin Yang, Yongjian Li, Changgeng Zhang, Baojun Qu, and Lei Cao. Anomalous loss modeling and validation of magnetic materials in electrical engineering. *IEEE Transactions on Applied Superconductivity*, 26(4):1–5, 2016.

[17] Seung Ryul Moon, Paul Ohodnicki, Kevin Byerly, and Richard Beddingfield. Soft Magnetic Materials Characterization for Power Electronics Applications and Advanced Data Sheets. In *2019 IEEE Energy Conversion Congress and Exposition (ECCE)*, pages 6628–6633, Baltimore, MD, USA, September 2019. IEEE.

[18] Dominik Neumayr, Dominik Bortis, Johann W. Kolar, Stefan Hoffmann, and Eckart Hoene. Origin and Quantification of Increased Core Loss in MnZn Ferrite Plates of a Multi-Gap Inductor. *CPSS Transactions on Power Electronics and Applications*, 4(1):72–93, March 2019.

[19] Daniela Rodriguez-Sotelo, Martin A. Rodriguez-Licea, Ismael Araujo-Vargas, Juan Prado-Olivarez, Alejandro Israel Barranco-Gutiérrez, and Francisco J. Perez-Pinal. Power losses models for magnetic cores: A review. *Micromachines*, 13, 3 2022.

[20] D.P. Rommel, Dario Di Maio, and Tiedo Tinga. Transformer hot spot temperature prediction based on basic operator information. *International Journal of Electrical Power and Energy Systems*, 124:106340, 01 2021.

[21] Marek S. Ryłko, Kelvin J. Hartnett, John G. Hayes, and Michael G. Egan. Magnetic material selection for high power high frequency inductors in DC-DC converters. In *Conference Proceedings - IEEE Applied Power Electronics Conference and Exposition - APEC*, pages 2043–2049, 2009.

[22] James Scoltock, Yiren Wang, Gerardo Calderon-Lopez, and Andrew J. Forsyth. Rapid thermal analysis of nanocrystalline inductors for converter optimization. *IEEE Journal of Emerging and Selected Topics in Power Electronics*, 8:2276–2284, 9 2020.

[23] S. D. Sudhoff. *Power Magnetic Devices: A Multi-Objective Design Approach*. IEEE Press, 2014.

[24] V.J. Thottuvelil, T.G. Wilson, and H.A. Owen. High-frequency measurement techniques for magnetic cores. *IEEE Transactions on Power Electronics*, 5(1):41–53, January 1990.

[25] A. Van den Bossche, V.C. Valchev, and G.B. Georgiev. Measurement and loss model of ferrites with non-sinusoidal waveforms. In *2004 IEEE 35th Annual Power Electronics Specialists Conference (IEEE Cat. No.04CH37551)*, volume 6, pages 4814–4818 Vol.6, 2004.

[26] Jian Wang, Heyun Lin, Yunkai Huang, and Xikai Sun. A new formulation of anisotropic equivalent conductivity in laminations. *IEEE Transactions on Magnetics*, 47:1378–1381, 2011.

[27] Yang Wang, Sajib Chakraborty, Dai Duong Tran, Thomas Geury, and Omar Hegazy. Design and optimization of the arm inductor for modular multilevel converter. In *2022 International Symposium on Power Electronics, Electrical Drives, Automation and Motion (SPEEDAM)*, pages 354–359, 2022.

[28] Yiren Wang, Gerardo Calderon-Lopez, and Andrew J. Forsyth. High-frequency gap losses in nanocrystalline cores. *IEEE Transactions on Power Electronics*, 32:4683–4690, 6 2017.

[29] Shuaichao Yue, Yongjian Li, Qingxin Yang, Xinran Yu, and Changgeng Zhang. Comparative analysis of core loss calculation methods for magnetic materials under non-sinusoidal excitations. *IEEE Transactions on Magnetics*, 54, 11 2018.